PERGAMON

Deep-Sea Research II 49 (2002) 1211–1230

DEEP-SEA RESEARCH
PART II

www.elsevier.com/locate/dsr2

The Ekman temperature and salt fluxes at 8°30′N in the Arabian Sea during the 1995 southwest monsoon

T.K. Chereskin[a,]*, W.D. Wilson[b], L.M. Beal[a]

[a] *Scripps Institution of Oceanography, La Jolla, CA 92093-0230, USA*
[b] *Atlantic Oceanographic and Meteorological Laboratory, Miami, FL 33124, USA*

Accepted 12 October 2001

Abstract

The Arabian Sea Ekman transport is an important component of the meridional overturning circulation of the Indian Ocean. Chereskin et al. (Geophys. Res. Lett. 24 (1997) 2541) presented direct estimates of the Ekman transport across latitude 8°30′N in the Arabian Sea for June and September during the 1995 southwest monsoon. In this paper, we use these measurements to determine the Ekman depth and the resultant heat and salt fluxes. In June, at the monsoon onset, the Ekman temperature and salt fluxes were estimated to be southward, 2.4 ± 0.4 PW and $0.71 \pm 0.1 \times 10^9$ kg s^{-1}. The transport-weighted Ekman temperature and salinity were 29.0 ± 0.5°C and 35.31 ± 0.03 psu, not significantly different from surface values, 29.2°C and 35.28 psu, respectively. In September at the end of the monsoon, the Ekman temperature and salt fluxes had decreased in magnitude but were still southward, 0.77 ± 0.4 PW and $0.27 \pm 0.1 \times 10^9$ kg s^{-1}. The transport-weighted temperature, 25.8 ± 0.5°C, was 1.1°C colder than the surface value, and the transport-weighted salinity, 35.83 ± 0.03 psu, was not significantly different from the surface value of 35.86 psu. For this pair of sections, the top of the pycnocline appeared to be a better approximation for the Ekman depth than either the mixed layer or a fixed depth, and our estimates of the Ekman heat and salt fluxes were integrated from the surface to the top of the pycnocline. Although uncertainty in the Ekman mass transport dominates the error in the Ekman heat and salt fluxes, determining the Ekman depth is also important in estimating the Ekman contribution to the heat budget of the tropical Indian Ocean. A decrease in Ekman temperature by 1.1°C resulted in a 5% decrease in the temperature transport estimated for September. © 2002 Elsevier Science Ltd. All rights reserved.

1. Introduction

The Arabian Sea is a natural laboratory for observing wind-driven circulation. It undergoes a dramatic annual reversal of both winds and currents due to the seasonal cycle of the monsoon winds. The reversing winds are accompanied by the annual reversal of the Somali Current at the western boundary and a reversal of the interior Arabian gyre circulation (see Schott and McCreary Jr. (2001) for a recent review). The amplitude of the annual cycle is not symmetric about zero; the summer southwest monsoon has stronger winds than the winter northeast monsoon. Therefore, the associated Ekman transport, southeastward in summer and northwestward in winter, is strongest during the summer monsoon, with a predicted southward maximum across latitude 8°30′N of about 20×10^6 m^3 s^{-1} (Fig. 1).

---

*Corresponding author. Fax: +1-858-534-7452.
E-mail address: tchereskin@ucsd.edu (T.K. Chereskin).

0967-0645/02/$ - see front matter
PII: S0967-0645(01)00168-0

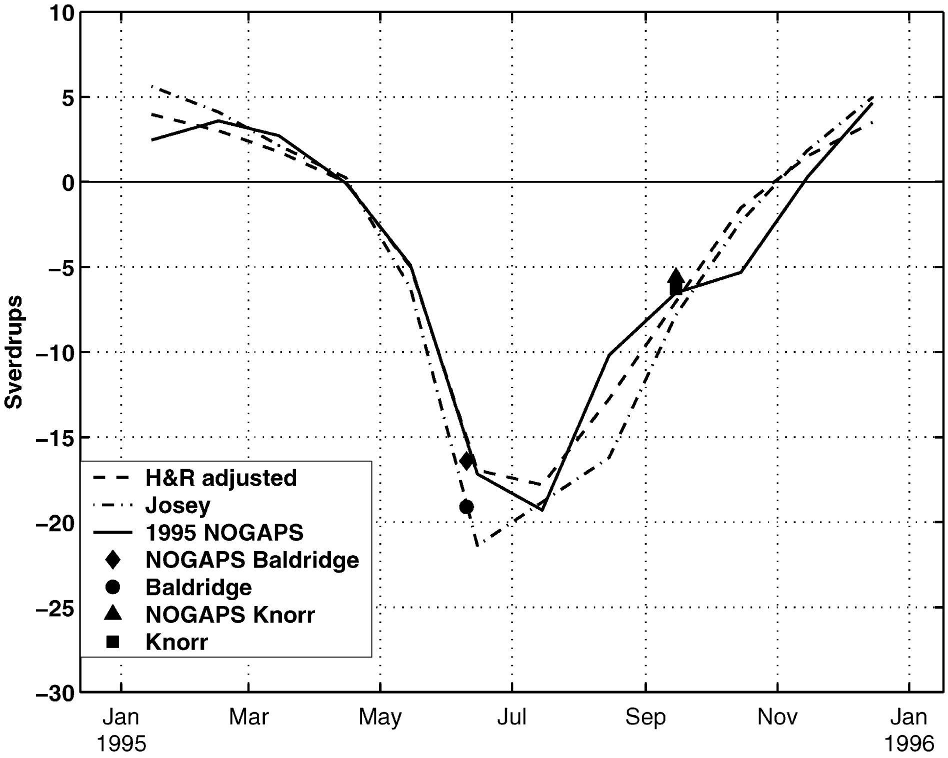

Fig. 1. Annual cycle of Ekman transport across 8°30′N in the Arabian Sea, from Hellerman and Rosenstein (1983) winds (drag coefficient adjusted to Large and Pond (1981) values), Josey et al. (1996) corrected COADS climatology, and 1995 FNOC NOGAPS. Estimates from ship winds and from NOGAPS interpolated to the ship track are shown as single point estimates at the midpoint of the cruise. Units are Sverdrups (1 Sv = 10^6 m^3 s^{-1}).

One of the surprising features of the summertime Arabian Sea circulation is the phenomenon of Arabian Sea cooling (Düing and Leetmaa, 1980); at a time when the net surface heat flux is at a maximum and directed into the ocean (Weller et al., 1996), the Arabian Sea experiences a rapid heat loss due primarily to the export of heat via the strong southeastward Ekman transport. Since the Ekman transport is large, carries the warmest water, and reverses seasonally, it can potentially reverse the sign of the net seasonal heat transport across latitude 8°30′N. Transport calculations from observations and model studies attest to the importance of the Ekman temperature flux in the meridional overturning circulation of the Indian Ocean (Wacongne and Pacanowski, 1996; Garternicht and Schott, 1997; Shi et al., 2001; Stramma et al., 2001). Analysis of the output of a global eddy-resolving model suggests that the annual cycle of heat flux in the northern Indian Ocean may be dominated by the Ekman temperature flux in the Arabian Sea (Garternicht and Schott, 1997). The Ekman temperature flux is sensitive to assumptions about the depth of penetration of the wind-driven flow, and therefore the Ekman depth as well as the Ekman transport are important issues for the meridional overturning circulation of the Indian Ocean.

For lack of a direct estimate, the Ekman transport has most often been inferred from wind-stress climatology (e.g., Hall and Bryden, 1982; Hellerman and Rosenstein, 1983; Levitus, 1987), with the disadvantages that the climatologies have large uncertainties and/or may not be representative of a particular period. Furthermore, indirect estimates from wind do not provide information on the vertical structure of the wind-driven currents. Recently, direct estimates of Ekman transport have been made by subtracting geostrophic currents from the total current estimated from shipboard acoustic Doppler current profiler (ADCP) measurements (Chereskin and Roemmich, 1991; Wijffels et al., 1994; Chereskin et al., 1997a). In addition to being concurrent with the hydrography, the Ekman transport estimated from ageostrophic velocity reveals the vertical structure of the wind-driven flow, its relation to the mixed layer, and its contribution to the heat and freshwater fluxes. Direct estimates of Ekman transport at 10°N in the Atlantic and Pacific Oceans are 12×10^6 m^3 s^{-1} and 62×10^6 m^3 s^{-1} northward, respectively (Chereskin and Roemmich, 1991; Wijffels et al., 1994). In the Atlantic, the Ekman layer temperature was 1°C colder than the surface mixed layer; in the Pacific, the Ekman temperature was not significantly different from the surface value. In both cases the Ekman transport extended beneath the mixed layer, to the top of the thermocline, and this depth was used by Wijffels et al. (1996) in their flux calculations. In the Indian Ocean, the Ekman transport could play an important role in the freshwater flux as well as the heat flux because of the subduction of saline surface water, Arabian Sea Water (ASW) in the northern Arabian Sea that advects southward during the summer monsoon (Morrison, 1997; Prasanna Kumar and Prasad, 1999). Since the subsurface waters at 8°30′N are in general colder and saltier than surface values, they can have a profound influence on the Ekman fluxes if the wind-driven flow penetrates deeply.

Chereskin et al. (1997a) presented direct estimates of the meridional component of the Ekman transport at latitude 8°30′N for June ($17.6 \pm 2.4 \times 10^6$ m^3 s^{-1} southward) and September ($7.9 \pm 2.7 \times 10^6$ m^3 s^{-1} southward) during the 1995 southwest monsoon. In this paper we use these measurements to examine changes in the surface layer between June and September and to estimate the Ekman depth and the Ekman contribution to the heat and freshwater fluxes.

2. Data

The observations used in this study consist of conductivity–temperature–depth (CTD), shipboard ADCP, and wind measurements on two cruises that made transects from Somalia to Sri Lanka as part of the World Ocean Circulation Experiment (WOCE). In addition, maps of sea level anomalies (MSLAs) are used to provide a plan view of the complex circulation in the Somali Current and Great Whirl region. The MSLAs were generated by the AVISO group from TOPEX/POSEIDON and ERS satellite altimetry observations http://www-aviso.cls.cnes.fr.

The locations of the CTD stations for the R.V. *Baldridge* (June 5–19, 1995) and the R.V. *Knorr* (September 12–26, 1995) are shown in Fig. 2. The June transect began at 51°E, 8°30′N and sampled due east. The section was closed off at Sri Lanka due to lack of clearance to sample within Indian territorial waters. The September transect began at 51°30′E, 9°30′N and sampled southeastward (orientation 38° clockwise from east) to 53°W, 8°30′N in order to cross the Somali Current perpendicular to the bathymetry; sampling was subsequently eastward except at the

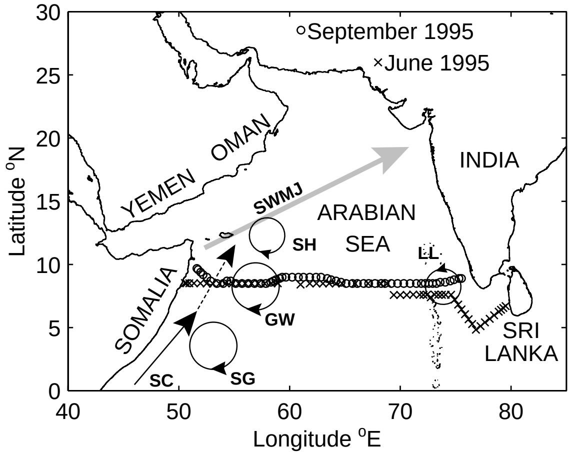

Fig. 2. Map showing the CTD station locations during June and September. Circulation features described in text are shown schematically: Southwest Monsoon Jet (SWMJ), Somali Current (SC), Southern Gyre (SG), Great Whirl (GW), Socotra High (SH), and Lakshadweep Low (LL). Adapted from Fig. 1 in Chereskin et al. (1997a).

Carlsberg Ridge where the track again deviated in order to cross orthogonal to the bathymetry. The section ends in shallow water off the west coast of India. For the June/September transect there are 57/59 stations, spaced approximately 60 km in mid-ocean and more closely near the coasts. The accuracies of the hydrographic measurements were 0.002°C, 0.004 PSS-78, and 3 dB, and the precisions were 0.001°C, 0.002 PSS-78, and 0.5 dB (Ffield et al., 1998).

Ship-relative wind speed and direction were measured and recorded at 1-min intervals from the ship's anemometer mounted on the mast about 20 m above sea level on the R.V. *Baldridge*. Ship-relative wind speed and direction at 1-min intervals on the R.V. *Knorr* were made from a wind sensor on an Improved Meteorological Recorder or IMET (Hosom et al., 1995) located forward on the bow about 16 m above sea level. Wind stress was computed using speed-dependent drag coefficients assuming a neutrally stable atmospheric boundary layer (Large and Pond, 1981). A bias correction of the wind sensor on the *R.V. Knorr* is discussed in the appendix and resulted in an adjustment of the wind magnitude for the underway periods of September 12–14. Although this correction was not applied by Chereskin et al. (1997a), it had a negligible effect on the transport, reducing the total to -6.3×10^6 m^3 s^{-1} from their published value of -6.4×10^6 m^3 s^{-1}.

Direct velocity measurements were made continuously along both ship tracks from depths of 14/21 m (*Baldridge*/*Knorr*) to roughly 400 m using hull-mounted shipboard ADCP. Both ships were equipped with 153.6 kHz narrowband units manufactured by RD Instruments. The units were configured to sample approximately every second using an 8-m vertical bin and an 8/16-m (*Baldridge*/*Knorr*) pulse. Absolute ocean currents were calculated by subtracting the ship velocity over the ground, determined from Global Positioning System (GPS) satellite position fixes, from the ship-relative current measured by the ADCP (Chereskin et al., 1997b; Ffield et al., 1998). Currents in the upper 20 m were estimated using a slab extrapolation, as in Chereskin et al. (1997a). The analysis presented here (Ekman transport and transport-weighted temperature and salinity) uses the ADCP relative velocities or shears and is insensitive to the errors from navigating the ship-relative currents to absolute velocity and to bias from heading errors. Error in the relative velocities averaged over steaming intervals between CTD stations (3–4 h) is less than 0.5 cm s^{-1} (Chereskin and Harding, 1993). Although the instrumental error is small, additional errors in estimating currents from shipboard ADCP arise from aliasing of unresolved high-frequency flows by the shipboard sampling, with the largest contribution to error in relative current or shear arising from high vertical wavenumber motion such as near-inertial waves. At latitude 8°30′N the inertial period is about 3.4 days and the horizontal wavelength is of order 500 km. Although the errors are reduced by averaging and most of our calculations are basin integrals, there are only about five inertial periods/wavelengths within these relatively short (about 3000 km) transects, compared to similar calculations made over much longer sections in the Atlantic and Pacific (Chereskin and Roemmich, 1991; Wijffels et al., 1994). Errors from unresolved current features such as near-inertial currents are the dominant contribution to the uncertainties in the transports (Chereskin et al., 1997a). An additional source of error in the transport arises from the extrapolation that is required for the unmeasured currents in the upper 20 m.

3. Observations of the surface layer at 8°30′N

3.1. Background

The southwest monsoon produces a low-level atmospheric jet (Findlater, 1969) that forms over Somalia sometime in May and extends out over the Arabian Sea in June, with orientation parallel to the coasts of Yemen and Oman (Fig. 2). The oceanic response to the monsoon onset, in particular the reversal of the Somali Current from a slow southward current to a northward flow with speeds in excess of 3 m s^{-1}, has been the focus of many modeling studies (e.g., Lighthill, 1969; Cox, 1979) that show the importance of both local and remote forcing. The Somali Current progresses northward as the monsoon intensifies, crossing the equator in May, 4°N in June, and 10°N in late August (Schott et al., 1990). Often in June the Somali Current feeds into an eastward offshore flow at about 4°N that forms the northern limb of an anticyclonic gyre known as the Southern Gyre. A second anticyclonic gyre known as the Great Whirl forms at latitudes 4°N–12°N off the Somali coast (Bruce, 1968; Schott and Quadfasel, 1982). A third anticyclonic gyre forms northeast of the island of Socotra during the late phase of the monsoon and is named the Socotra High (Bruce, 1979). The cyclonic Lakshadweep Low forms in the southeastern Arabian Sea, off the southwest tip of India (Bruce, 1968; Shankar and Shetye, 1997). Few measurements have been made close to Somalia in recent times because of political turmoil there; hence one outstanding question is how much communication occurs between the coastal Somali Current and the Arabian Sea. Significant northward flow has been observed in the deep passage between Somalia and Socotra (about 13×10^6 m^3 s^{-1}) and to the east of the Great Whirl (Fischer et al., 1996; Schott et al., 1997). The transport of the Great Whirl was

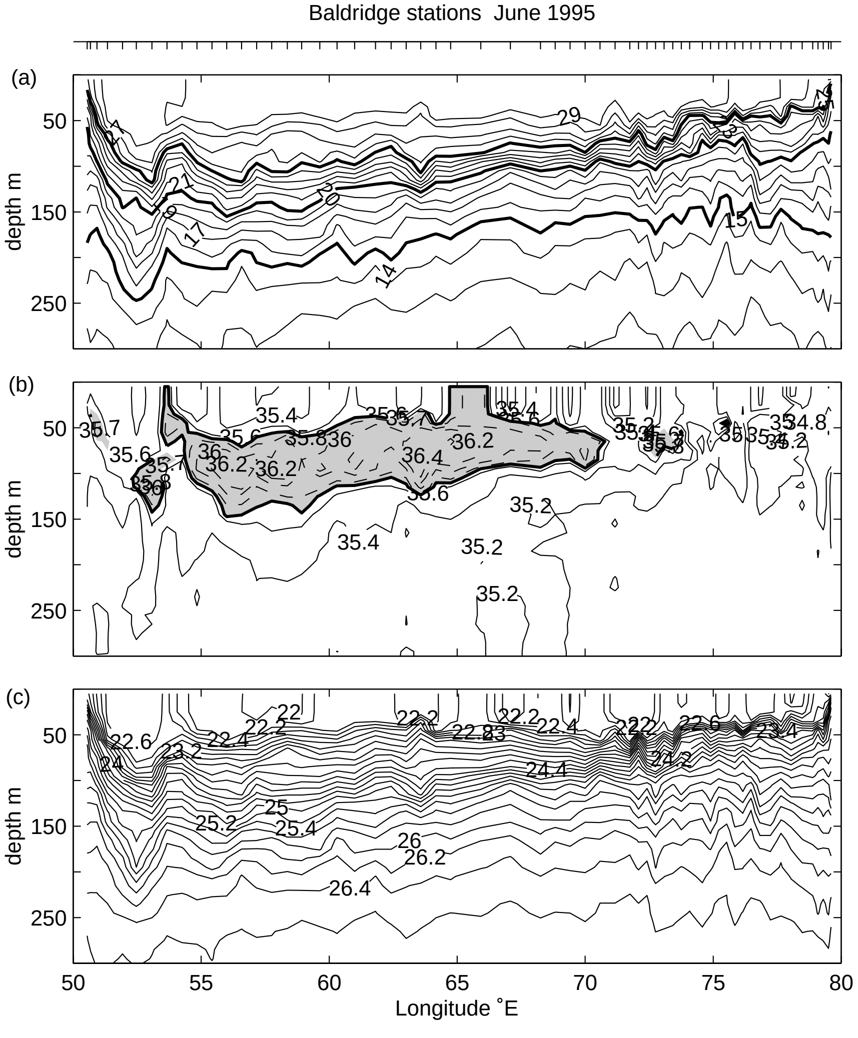

Fig. 3. (a) Temperature, °C, (b) salinity, psu, and (c) sigma-theta, kg m^{-3}, during June 1995. Salinities greater than 35.7 psu are shaded. Ticks on the top axis mark locations of CTD stations.

estimated by Fischer et al., (1996) at $58 \times 10^6\ \mathrm{m}^3\ \mathrm{s}^{-1}$, but appeared to recirculate locally.

Statistically, the 1995 southwest monsoon was typical, with monthly averages of meterological variables and fluxes made from buoy measurements located near 15°N, 62°W within one standard deviation of climatological means, although the timing and character of the 1995 onset were different from other years (Weller et al., 1996). There was a double onset, with an initial wind burst in mid-May followed by a break; the full-strength winds developed about a week later than usual, around 10 June (Schott et al., 1997). Surface current observations indicated that the Great Whirl had developed by June (Schott et al., 1997). By August, the Socotra High was also evident, and the Great Whirl had increased in size and strength. Moored measurements over the eastern half of the Socotra Passage indicated northward transport throughout most of 1995 (Schott et al., 1997).

3.2. Hydrography

Consistent with the progression of the southwest monsoon, the vertical structure of the surface layer changed markedly between June and September. In June, the surface layer was very warm, with mean surface temperature of 29.2°C and mean surface salinity of 35.29 psu (Figs. 3a and b). A subsurface salinity maximum layer of ASW with salinity greater than 35.7 psu was centered at approximately 80 m depth and extended from 52°E to 70°E (Fig. 3b). The main pycnocline was shallow, centered around 100 m depth, with a pycnocline bowl corresponding to the anticyclonic Great Whirl evident against the western boundary (Fig. 3c). Isopycnal spreading at the eastern boundary, centered at 100 m, indicates the presence of a poleward undercurrent that carries low-salinity water from the southwestern Bay of Bengal (Shetye et al., 1990).

In September, the surface-layer temperatures were considerably cooler and salinities were higher than in June, with a mean surface temperature of 27.6°C and mean surface salinity of 35.98 psu (Figs. 4a and b). A strong narrow northeastward flow (the Somali Current) is apparent at the western boundary, separated from the Great Whirl by a counterflow to the southwest. The Great Whirl is considerably larger than in June and now extends over roughly 5° of longitude, from 52°30′E to 57°30′E (Fig. 4c). Relatively fresh Indian Equatorial Water (IEW) with salinity about 35.4 psu flows northward at the western boundary in the Somali Current and recirculates in the Great Whirl (Fischer et al., 1996; Schott et al., 1997). The ASW layer seen in June has shifted to the east and now extends from the surface to about 100 m depth (Fig. 4b). The doming of isopycnals associated with the Lakshadweep Low is apparent at the eastern boundary.

3.3. Currents

Absolute velocities for June and September at a depth of 22 m are shown in Figs. 5 and 6, overlain on maps of sea-level anomaly http://www-aviso.cls.cnes.fr. The scale for the currents is set by the large currents at the western boundary. The MSLAs were chosen at the times closest to sampling at the western boundary, and the insets show an expanded view of the Somali Current–Great Whirl region. The Great Whirl is apparent as a relative maximum in the sea-surface height; a sequence of MSLAs (not shown) indicates high-frequency temporal variability in the height anomaly field that intensifies at the western boundary. In June the anticyclonic Great Whirl lies between the Somali coast and 54°W. There is an asymmetry in the gyre, with the NNE flow off Somalia having much greater speeds, in excess of $1.5\ \mathrm{m\ s}^{-1}$, than the SSW flow that closes the gyre more broadly to the east. The gyre centre is just west of 53°W, and there is a narrow band of flow, due south, at 53°W with speeds approaching $1.0\ \mathrm{m\ s}^{-1}$; flow further to the east has a considerable westward component. The surface-current direction closely parallels the sea-surface height anomaly contours near the western boundary (Fig. 5 inset). The coastal Somali Current either did not extend as far north as 8°30′N in June, or it was inshore of the westernmost CTD station (Beal and Chereskin, 2001). The southward flow observed in the interior of the basin will be shown

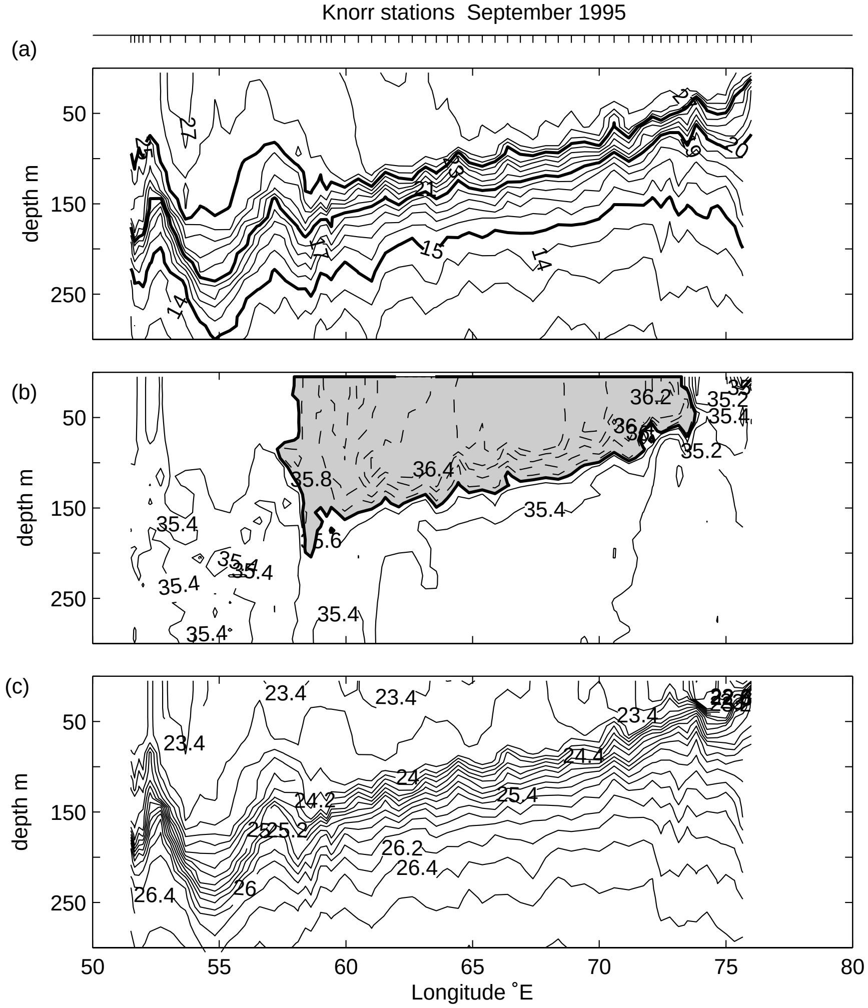

Fig. 4. (a) Temperature, °C, (b) salinity, psu, and (c) sigma-theta, kg m^{-3}, during September 1995. Salinities greater than 35.7 psu are shaded. Ticks on the top axis mark locations of CTD stations.

to be primarily wind-driven (Section 4). The Lakshadweep Low off the southeast coast of India is not well measured by this section, which passes to the south of India and terminates at Sri Lanka.

In September, there is a separation between a strong northward-flowing western boundary jet and the recirculating Great Whirl (Fig. 6 inset). The MSLA shows that the height-anomaly maximum corresponding to the Great Whirl lies between two minima at the time of the transect (Fig. 6). The surface current directions align extremely well with the height-anomaly contours, indicating that the large westward component of the flow between the Great Whirl and the Somali Current is part of a cyclonic circulation to the south and west of the Great Whirl (Fig. 6 inset). The coastal jet is extremely narrow, yet carries considerable transport; integrating the shipboard ADCP from the coast to 100 km offshore and from the surface to about 400 m depth yields a transport of $24 \pm 1.5 \times 10^6$ m^3 s^{-1}. This surface layer estimate does not include a significant deep transport of about 13×10^6 m^3 s^{-1} that extended to about 2000 m and was captured by the lowered

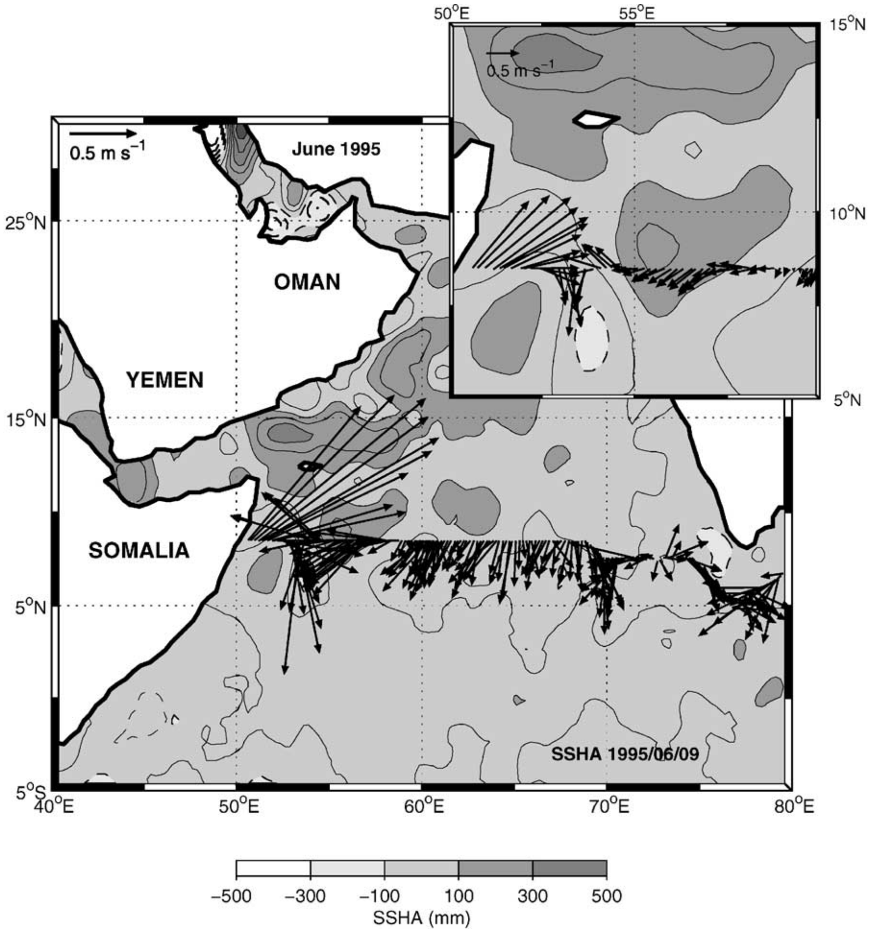

Fig. 5. Shipboard ADCP vectors at 22 m, block-averaged every 20 km, measured from the R.V. *Baldridge* on the WOCE IR1 line during June 1995 overlain on the map of sea level anomaly (MLSA) for June 9. (MLSA produced by AVISO). Inset provides an expanded view of the Great Whirl.

ADCP measurements (Beal and Chereskin, 2001). This large coastal transport is consistent with prior observations of northward flow entering the Arabian Sea via the Somali–Socotra Passage (Fischer et al., 1996; Schott et al., 1997) and suggests that transport through the shallow westward Somali shelf side of the passage may be non-negligible. The velocities in the salinity maximum layer in the eastern part of the section appear quite small by comparison, but they are still considerable, of order 0.2 m s^{-1} southward. The cyclonic flow of the Lakshadweep Low is apparent at the eastern boundary, with northward flow at the coast and interior southward flow from the surface to a depth of 150 m.

3.4. Winds

Wind velocity vectors in June revealed average wind speeds that exceeded 10 m s^{-1} at the western boundary (Fig. 7a), which was in closest proximity to the core of the atmospheric southwest monsoon jet. Although the wind magnitude in June decreased in mid-basin relative to the western boundary, the wind direction rotated from NNE (mostly cross-track) to ENE (mostly along-track),

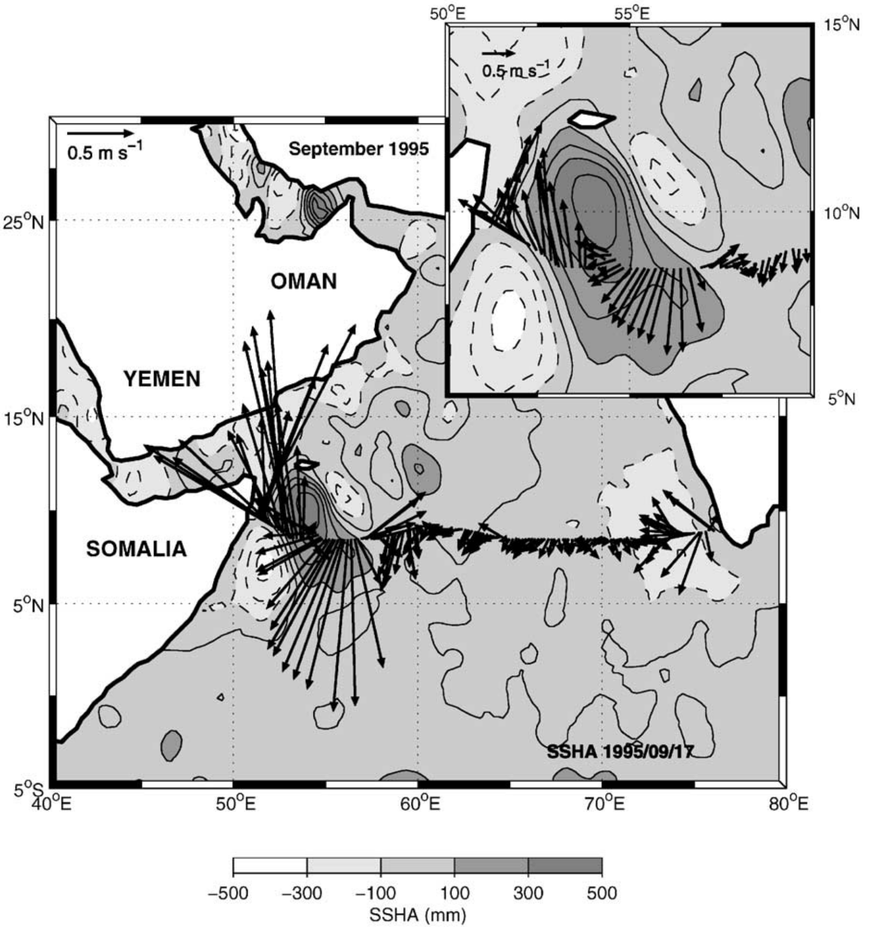

Fig. 6. Shipboard ADCP vectors at 21 m, block-averaged every 20 km, measured from the R.V. *Knorr* on the WOCE I1 line during September 1995 overlain on the map of sea level anomaly (MLSA) for September 17. (MLSA produced by AVISO). Inset provides an expanded view of the Somali Current and Great Whirl.

and so the southward Ekman transport (driven by the along-track wind stress) is predicted to be about as large in mid-basin as at the western boundary despite weaker wind speed. The maximum winds at the western boundary are still strong in September (Fig. 7b), but the magnitude decays rapidly to the east and the wind vector rotates anticyclonically such that there is a negative wind stress curl pattern centered on mid-basin. The wind pattern suggests that the amplitude of the southward component of the Ekman transport should decrease to zero at 65°E and then increase further to the east (still southward).

4. Distribution of the Ekman transport

The Ekman transport relation predicts the cross-track component of the Ekman transport $\int v_{\mathrm{E}}\,\mathrm{d}z$ from the along-track surface wind stress τ_0^x,

$$\int_{-H}^{0} v_{\mathrm{E}}\,\mathrm{d}z = \frac{-\tau_0^x}{\rho f}, \qquad (1)$$

where v_{E} is the ageostrophic wind-driven velocity in the Ekman layer, H is the Ekman depth, ρ is the water density, and f is the Coriolis parameter. Integrating (1) across the width of the Arabian Sea yields the meridional component of the Ekman volume transport, M_{Ek}^y. Because wind

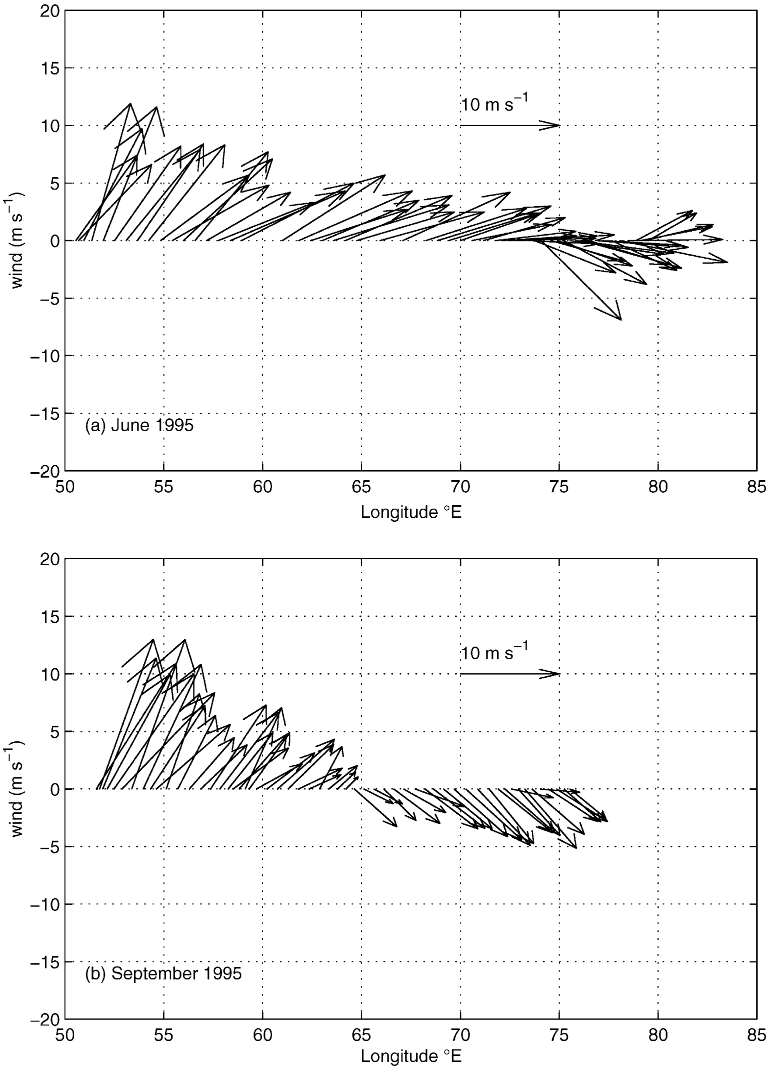

Fig. 7. (a) Shipboard wind vectors, averaged between station intervals, measured from the R.V. *Baldridge* on the WOCE IR1 line during June 1995. (b) Shipboard wind vectors, averaged between station intervals, measured from the R.V. *Knorr* on the WOCE I1 line during September 1995.

measurements are more widely available than currents (especially the ageostrophic component of current), the Ekman transport is usually estimated from the right-hand side of (1). We will refer to estimates of Ekman transports based on the right-hand side of (1) as indirect or wind estimates (M^y_{indirect}), because they infer oceanic transports from atmospheric forcing. Our wind estimates will use the shipboard winds since they are synoptic with the current observations and show good agreement with climatology and with other 1995 estimates (Fig. 1). We will refer to transport estimates calculated using ageostrophic velocity in the left-hand side of (1) as direct estimates (M^y_{direct}).

Our transport calculations differ from Chereskin et al. (1997a) in our choice of integration limits. They integrated (1) from 50°E to 77°E. These limits made the sections comparable in length but did not close off the June section to the east at a land boundary. For the temperature and salt flux calculations it is desirable to close off the Arabian Sea to the north. Integrating the June section beyond 77°E to 80°E resulted in increased magnitudes of M^y_{direct} (-18.3 compared to $-17.6 \times 10^6\ \text{m}^3\ \text{s}^{-1}$) and M^y_{indirect} (-20.8 compared to $-19.1 \times 10^6\ \text{m}^3\ \text{s}^{-1}$) with $H = 160$. The second change in our calculation is in the choice of the Ekman depth. Chereskin et al. (1997a) integrated both sections from the surface to 160 m in order to have a common integration depth. The Ekman heat and salt fluxes are much more sensitive to assumptions about the Ekman depth than the Ekman mass flux, and the main goal of this section is to determine the appropriate Ekman depth H.

We first thought that we could define the Ekman depth as the depth for which the depth-integrated ageostrophic velocity profile matched the wind estimate. However, on a station pair basis, the velocities are too noisy, although basin-integrals yield reasonable signal-to-noise in the net transports. The ageostrophic velocity sections, contoured from the unsmoothed station pair data, give a qualitative look at the signal-to-noise in the currents (Figs. 8 and 9). The dominant surface-intensified southward flow is evident in each case, as is the background noise from other ageostrophic currents such as near-inertial waves. In particular, although the sign of the Ekman transport predicted from the shipboard winds is always southward (the winds always have an eastward componenent in Fig. 7), the ageostrophic currents are at times northward, and these northward currents are the "noise" for this calculation, presumably due to nonwind-driven flows.

Our second approach was to relate the Ekman depth to the density field, using both the pattern of ageostrophic currents and the wind estimate of Ekman transport as constraints. The Ekman depths should mirror the pattern of southward ageostrophic flow (deepening to the west) and must yield transports that match the total (Fig. 10) and the horizontal distribution (Fig. 11) of Ekman transport within the error bars on the calculation (about 20% of the wind estimate). One advantage of this approach is that, if verified, it can be

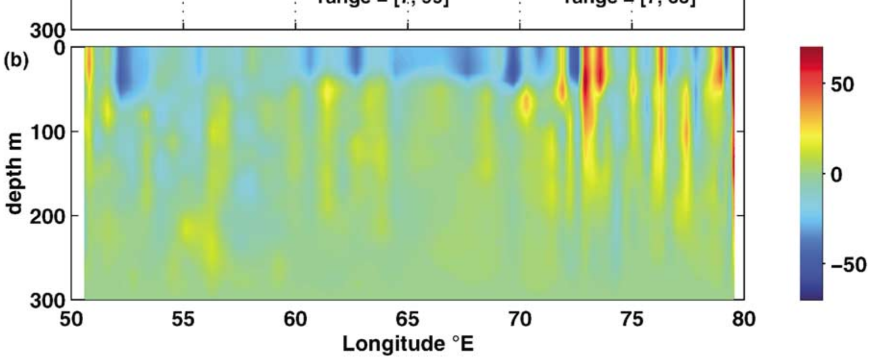

Fig. 8. (a) The depths of the mixed layer (shaded circles, MLD) and the top of the pycnocline (filled triangles, TTP) and (b) the ageostrophic current (cm s^{-1}) estimated for June.

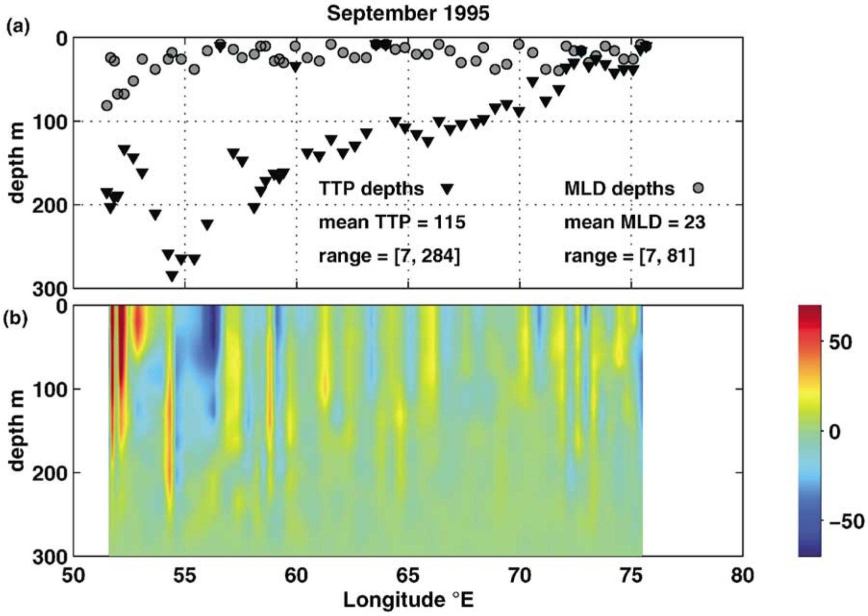

Fig. 9. (a) The depths of the mixed layer (shaded circles, MLD) and the top of the pycnocline (filled triangles, TTP) and (b) the ageostrophic current (cm s^{-1}) estimated for September.

applied to historical datasets where only density and wind observations are available.

We followed Wijffels et al. (1994) in defining the mixed-layer depth (MLD) as the depth at which the density changed by 0.01 kg m^{-3} from its value at 6 m (a depth below diurnal influence) and the top of the pycnocline (TTP) as the shallowest depth at which the density gradient was greater than or equal to 0.01 kg m^{-4} (Figs. 8 and 9). The TTP extends down through the weakly stratified transition zone between the base of the mixed layer and the pycnocline. For example, comparing Figs. 9 and 4a one can see that the temperature decreases by more than 1°C from the surface to the TTP; the mean decrease is 4.5°C and the maximum, at 55°E, is 10.5°C. Since it is a gradient criterion, the TTP defines regions of weaker stratification rather than a particular density surface. We hypothesize that some fraction of the wind momentum is mixed down into the transition zone, and the TTP appears to approximate the depth of the wind mixing. The MLD is not very different between June and September, with mean MLDs of 29 and 23 m, respectively. In June the MLD is often as deep as the TTP, except near the western boundary where the TTP is about twice as deep. The mean TTP for June is 46 m. In September, although there are a few instances where the TTP is as shallow as the MLD, the TTP is generally much deeper, with a mean of 115 m and a maximum of 284 m. In particular, the TTP captures the dramatic deepening at the western boundary that developed between June and September.

The TTP depth does a good job of capturing the pattern of depth distribution of the ageostrophic flow. In June the currents in the surface layer were strongly southward across most of the section (Fig. 5), whereas the density-driven geostrophic flow relative to 300 m was weakly sheared and northward (Chereskin et al. 1997a). The total current was dominated by the ageostrophic flow. Examining the transport as a function of integration depth shows that virtually all of the ageostrophic transport was confined to the upper 50 m in June (Fig. 10a), above the core of the ASW layer (Fig. 3b). The geostrophic transport increased with integration below 50 m, but that transport increase was mirrored in the total current transport and therefore there was

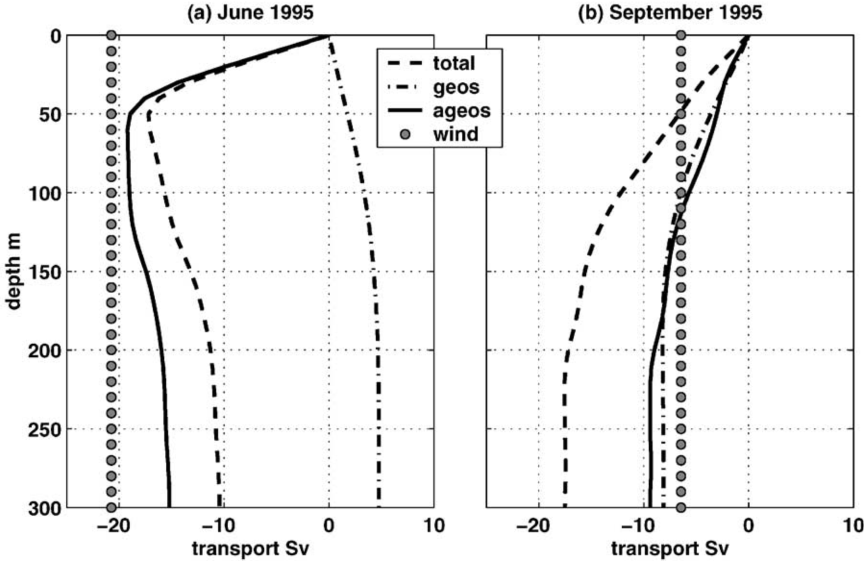

Fig. 10. Cumulative basin-integrated transport versus integration depth for (a) June and (b) September 1995. Solid curve is the ageostrophic transport. Dashed curve is the ADCP transport. Dash–dot curve is the geostrophic transport. Velocities were referenced to 300 m. The Ekman transport estimated from the shipboard winds from each section is shown as a constant level (shaded circles). Units are Sv (1 Sv = 10^6 m^3 s^{-1}).

negligible increase in the ageostrophic transport. The depth distribution indicates 50 m as an appropriate maximum depth, and this depth is approximately the mean TTP depth. Integrating from the surface to the TTP also gives the best agreement for the horizontal distribution of transport (Fig. 11a). The transport associated with the Great Whirl was in geostrophic balance, and therefore did not contribute to the ageostrophic transport. The ageostrophic transport increased approximately linearly across the basin, from 50°E to 73°E, where it reached a maximum of about 20×10^6 m^3 s^{-1} southward (Fig. 11a). The ageostrophic transport matches that estimated from the ship winds over most of the basin. Integrating to 160 m depth (not shown), the ageostrophic transport exceeds the wind estimate over most of the basin, reaching a maximum of 25×10^6 m^3 s^{-1} at 73°E before dropping back to about 20×10^6 m^3 s^{-1}. Although choosing the TTP as the Ekman depth improves the fit to both the vertical and horizontal distribution of the transport, within the error bars on the calculation (about 20% of the wind estimate), the totals in mass transport are indistinguishable over the range of depths from 50 to 160 m. However, the Ekman heat and salt transports are sensitive to this depth, and choosing the shallowest consistent Ekman depth is the most conservative assumption for these transports.

In September the flow had a very pronounced deepening in the west, to about 200 m, and shallowed approximately linearly until about 70°E (Fig. 9). The transport in September was about one half of the June value, but it extended about three times as deep (Fig. 10b), and the stratification was weaker (Fig. 4). The total, geostrophic, and ageostrophic transports relative to 300 m were all southward, with the ageostrophic and the geostrophic shears each contributing about 50% to the total shear (Fig. 10b). The deepening of the pycnocline in the west by more than 100 m between June and September (Figs. 3c, 4c) resulted in a basin-wide tilt from east to west. This mean tilt indicates that the geostrophic southward flow was a basin-wide feature—the interior flow of the Arabian Sea exiting south—transporting saline ASW towards the equator (Fig. 4b). All three transports accumulate with

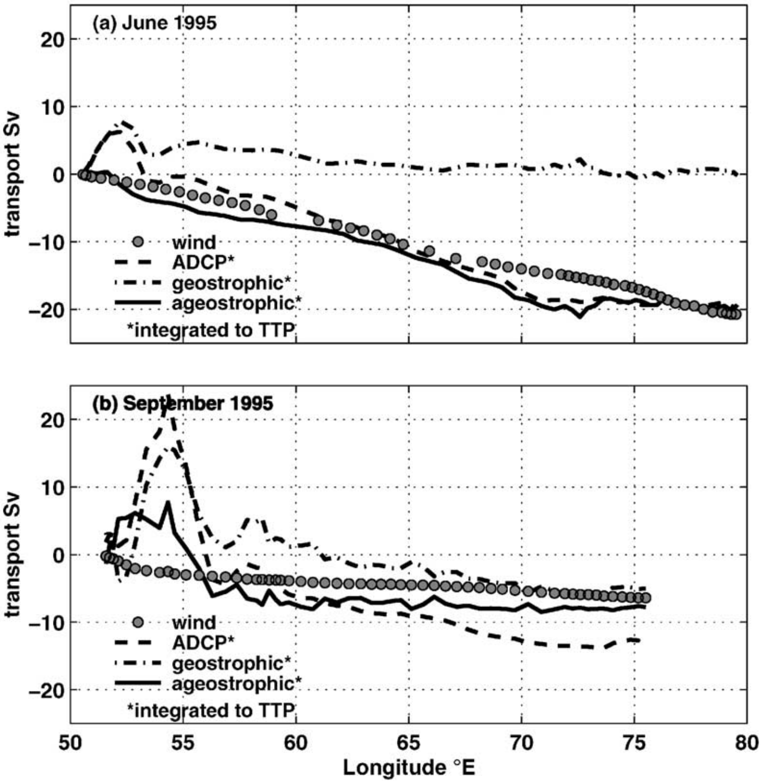

Fig. 11. Cumulative transport along the ship track for (a) June and (b) September 1995. Direct estimates were integrated from the surface to the TTP. Units are Sv (1 Sv = 10^6 m^3 s^{-1}).

integration depth until about 150 m depth, where all three flatten out (Fig. 10b). The ageostrophic transport captures the wind estimate total at about 115 m, the mean TTP depth (Fig. 9). The cumulative transport across the section (Fig. 11b) begins with the first CTD station, located at 51°30′E, offshore of the narrow northward coastal jet observed with shipboard ADCP (Fig. 6). The CTD station spacing may be inadequate to capture the intense narrow western boundary flow adequately, and the mismatch in resolution between ADCP and CTD observations may account for some of the northward ageostrophic transport that accumulates initially (Fig. 11b). Other possible explanations are that 300 m is not a deep enough reference level at the western boundary or that the ageostrophic flow is real but not wind-driven, for example, due to nonlinearity of the Great Whirl. As in June there is a recirculating transport in the Great Whirl. The recirculation has roughly doubled in horizontal extent, and there is some suggestion of nonlinear cyclostrophic flow, with total currents measured by ADCP slightly larger than the geostrophic estimates, unlike in June when the Great Whirl currents were geostrophically balanced. The cyclostrophic effect is cancelled by symmetry in the integral (Fig. 11b), and the cumulative ageostrophic velocity gets reset, passing through zero to the east of the Great Whirl. After the anomalous northward ageostrophic transport, the ageostrophic transport remains southward along the rest of the section, and it accumulates more rapidly than the estimate based on the wind. The slope of the cumulative transport predicted by the wind flattens out near 65°E where the along-track wind stress passes through zero (Figs. 7b, 11b). The slope of the cumulative ageostrophic transport is in reasonable agreement with the wind estimate but has more variability, due to noise in the velocity estimates. The patterns of accumulation match reasonably well east of the Great Whirl (Fig. 11b). The rate of transport accumulation is smaller in the eastern basin, corresponding to smaller along-track winds and southward currents (Figs. 6, 7b). For the September transect, using the TTP is not appreciably different from using 160 m for the volume, heat, or salt fluxes.

5. Ekman temperature and salinity transports

We define the Ekman temperature H_E and salt S_E fluxes as

$$H_E = \rho C_p \int_{x_1}^{x_2} \int_{-H}^{0} T v_E \, dz \, dx,$$
$$S_E = \rho \int_{x_1}^{x_2} \int_{-H}^{0} s v_E \, dz \, dx, \tag{2}$$

where C_p is the specific heat capacity of sea water at constant pressure (assumed constant at 4000 J kg^{-1} °C^{-1}), density ρ is assumed constant at 1025 kg m^{-3}, v_E is the velocity in the Ekman layer (estimated both from wind and ageostrophic velocity), T is the measured temperature, and S is the measured salinity. It is useful to think of the fluxes in terms of an Ekman layer with mean temperature θ_E and salinity s_E; the Ekman temperature and salt fluxes are then the product of the Ekman volume transport M_{Ek}^y and the transport-weighted Ekman temperature and salinity, respectively:

$$H_E = \rho C_p \theta_E M_{Ek}^y, \quad S_E = \rho s_E M_{Ek}^y. \tag{3}$$

In the previous section, we found that the depth of the TTP best described the vertical extent of the wind-driven flow for both sets of observations; using the TTP for the Ekman depth $H(x)$ and the ageostrophic velocity for v_E will yield our best direct estimate of the Ekman temperature and salt fluxes (referred to as direct TTP below and in Table 1). For comparison, we also calculated the fluxes using surface values for T and S (the direct surface calculation). A comparison of these two direct calculations shows how significant the assumption about the Ekman depth is for the heat and salt fluxes. The second calculation is also useful for comparison with prior studies (e.g., Levitus, 1987). However, since most other studies do not have available direct velocity measurements and instead use (1) to infer the mass transport from the wind, it is also instructive to calculate and compare the Ekman heat and salt fluxes using the wind estimates of Ekman transport, for the same pair of assumptions about the Ekman depth, that is for the TTP and the surface. These calculations are referred to as indirect TTP and indirect surface. Finally, a number of studies have chosen some constant Ekman depth such as 50 m (e.g., Hall and Bryden, 1982; Stramma et al., 2001) for averaging the temperature, referred to in Table 1 as the indirect layer calculation. The five different calculations are described in detail below and summarized in Table 1. The temperature calculation for each method is stated explicitly; the salinity calculation is analogous.

5.1. The direct TTP calculation

$$\theta_E = \frac{\int \int_{-TTP}^{0} T(x,z) v_{ageos}(x,z) \, dz \, dx}{M_{direct}^y}. \tag{4}$$

The direct TTP calculation (Table 1) uses the measured temperature and salinity and the ageostrophic velocity, integrated to the TTP for both June (Fig. 8) and September (Fig. 9). Using the ageostrophic velocity as the appropriate vertical weighting involves the least assumption about the vertical penetration of the wind-driven flow but also includes the most noise. As previously noted, the magnitude of the noise can be observed in the occurrence of northward ageostrophic velocities (Figs. 8 and 9) whereas the wind predicts the Ekman transport to be unidirectional and southward. To estimate the uncertainty in the direct estimates, we also computed (4) using only southward ageostrophic velocity in both numerator and denominator. The uncertainties were estimated to be 0.5°C for the Ekman temperature and 0.03 psu for the Ekman salinity for both June and September calculations.

Table 1
The transport-weighted temperature θ_E(°C) and salinity s_E (psu) in the Ekman layer calculated using five different methods as described in the text, and the associated Ekman volume M_{Ek} (10^6 m^3 s^{-1}), temperature H_E (PW), and salt S_E(10^9 kg s^{-1}) fluxes[1]

Method	June					September				
	θ_E	s_E	M_{Ek}	H_E	S_E	θ_E	s_E	M_{Ek}	H_E	S_E
Direct										
TTP	29.0	35.31	−19.7	−2.35	−0.71	25.8	35.83	−7.3	−0.77	−0.27
Surface	29.2	35.28	−19.7	−2.36	−0.71	26.9	35.86	−7.3	−0.81	−0.27
Indirect										
TTP	28.8	35.37	−20.8	−2.45	−0.75	25.4	35.79	−6.3	−0.66	−0.23
Surface	29.2	35.28	−20.8	−2.49	−0.75	27.1	35.85	−6.3	−0.70	−0.23
Layer	28.5	35.40	−20.8	−2.43	−0.75	26.9	35.86	−6.3	−0.69	−0.23

[1] The flux calculation assumed a constant value of $\rho = 1025$ kg m^{-3} and $C_p = 4000$ J kg^{-1} °C^{-1}. Uncertainties in the transport-weighted temperature and salinity are 0.5°C and 0.03 psu, respectively. Uncertainties in the volume, temperature, and salt fluxes are 2.4×10^6 m^3 s^{-1}, 0.4 PW, and 0.1×10^9 kg s^{-1}, respectively.

5.2. The direct surface calculation

$$\theta_E = \frac{\int T(z=0) \int_{-\mathrm{TTP}}^{0} v_{\mathrm{ageos}}(x,z)\,\mathrm{d}z\,\mathrm{d}x}{M^y_{\mathrm{direct}}}. \tag{5}$$

We repeated the direct calculation using the mean surface temperature and salinity for each CTD station interval, with v_{ageos} as a weighting for the horizontal distribution of the transport. A comparison with the direct TTP estimate (Table 1) indicates the change in the Ekman temperature and salt fluxes due to the deep penetration of the ageostrophic flow.

5.3. The indirect TTP calculation

$$\theta_E = \frac{\int [0.67 \times T(z=0) + 0.33 \times T(z=TTP)](-\tau_0^x/\rho f)\,\mathrm{d}x}{M^y_{\mathrm{indirect}}}. \tag{6}$$

Wijffels et al. (1996) used a linear profile of Ekman velocity between the surface and the TTP depth to estimate the Ekman fluxes along 10°N in the Pacific. For this indirect calculation, we used the Ekman transport inferred from the in situ wind for the horizontal weighting and assumed the Ekman velocity was linearly distributed between the surface and the TTP depths (Figs. 8 and 9). This calculation provides a good counterpoint to the direct TTP calculation, in that it is independent of the ageostrophic velocity. Note that the Ekman mass flux calculated from the wind (Table 1) differs from the direct estimate.

5.4. The indirect surface calculation

$$\theta_E = \frac{\int T(z=0)(-\tau_0^x/\rho f)\,\mathrm{d}x}{M^y_{\mathrm{indirect}}}. \tag{7}$$

A common method in the calculation of oceanic heat transport estimates the Ekman transport from the wind and uses the surface temperature and salinity for the Ekman heat and salt fluxes (e.g., Levitus, 1987). Hence, this calculation provides a comparison with historical results and tests the sensitivity of the Ekman depth assumption for the indirect calculation (Table 1).

5.5. The indirect layer calculation

$$\theta_E = \frac{\int [0.67 \times T(z=0) + 0.33 \times T(z=50m)](-\tau_0^x/\rho f)\,\mathrm{d}x}{M^y_{\mathrm{indirect}}}. \tag{8}$$

A number of calculations of oceanic heat transport have estimated the Ekman transport from the wind and assumed that its distribution decays linearly from the surface to some fixed depth H, with 50 m a common choice (e.g., Hall and Bryden, 1982; Stramma et al., 2001). For comparison, we repeated the calculation using the wind estimates and assuming a linear weighting of temperature and salinity with depth.

5.6. Results

In June the direct TTP method gives an Ekman temperature of 29.0 ± 0.5°C and an Ekman salinity of 35.31 ± 0.03 psu. However, none of the various estimates of the Ekman temperature and salinity is significantly different from the basin-averaged surface values (29.2°C and 35.28 psu, Table 1). The layer calculation yields the most extreme values of temperature (28.5°C) and salinity (35.40 psu), primarily because it gives undue weighting to the region of shallow pycnocline at the eastern boundary. The temperature flux is estimated to be 2.4 ± 0.4 PW southward, and the large error bar is dominated by the 2.4 Sv uncertainty in the mass transport. The indirect TTP method yielded an Ekman temperature and salinity in good agreement with the direct method, but the temperature transports differ by about 0.1 PW primarily due to the difference in volume transport. The salt flux is estimated to be $0.71 \pm 0.1 \times 10^9$ kg s^{-1}.

In September, both the direct and indirect estimates indicate that the Ekman temperature was about 1.1 ± 0.5°C colder than the basin-averaged surface temperature (26.9°C), and the Ekman salinity was about 0.03 ± 0.03 psu fresher than the surface value (35.86 psu). The temperature transport was 0.77 ± 0.4 PW southward, and as in June the large error bar is due primarily to the 2.7 Sv uncertainty in the volume transport. For a fixed volume transport (i.e. examining either the direct or indirect calculation), one can see that there is a significant reduction in the Ekman temperature flux, about 5% less than that inferred using the surface temperature. This reduction becomes more significant when one considers heat flux rather than temperature flux, because the net heat flux is the residual of the sum of the temperature fluxes of the Ekman, western boundary current, and geostrophic components. For example, we can put an upper bound on the heat transported by the ocean across 8°30′N by assuming that the ocean transports all the heat gained from the atmosphere (no storage). In September 1995 the Arabian Sea north of 8°30′N gained 0.32 PW based on the SOC climatology (S. Josey, pers. comm.). The reduction in the Ekman component due to the Ekman layer being 1°C colder than surface is then about 12%. The decrease in the Ekman salinity above the surface mixed-layer value in September had a negligible effect on the salt flux, which was -0.27×10^9 kg s^{-1}. We speculate that the significant deviation of the Ekman temperature from surface values in the Atlantic and Indian Oceans may result from greater influence of the western boundary deepening in the averages over these small basins. For instance, the western deepening of the TTP occupied roughly half the September section, whereas it occupied a relatively small portion of the June section and represents a tiny portion of the 10,000 km section at 10°N in the Pacific.

6. Discussion and summary

We expect the Ekman transport to play a significant role in the heat and freshwater budgets at tropical latitudes because the wind-driven transport is large, penetrates relatively deep due to large forcing and small f, and the tropical thermocline is shallow. Shipboard observations of winds and upper ocean currents from a pair of hydrographic/ADCP transects of the Arabian Sea at latitude 8°30′N were used to determine the depth of penetration of the wind-driven flow and to estimate the Ekman temperature and salt fluxes. In June, at the monsoon onset, the Ekman temperature and salt fluxes were estimated to be southward, 2.4 PW and 0.71×10^9 kg s^{-1}. The surface layer was strongly stratified, and the depths of the mixed layer and the top of the pycnocline were very similar except at the western boundary where the pycnocline deepened. The transport-weighted Ekman temperature and salinity were 29.0 ± 0.5°C and 35.31 ± 0.03 psu, not significantly different from surface values, 29.2°C and 35.28 psu, respectively.

In September, at the end of the monsoon, the Ekman temperature and salt fluxes had decreased in magnitude but were still southward, 0.77 PW and 0.27×10^9 kg s^{-1}. The large decrease in these fluxes is due both to a decreased Ekman transport (Chereskin et al., 1997a) as the monsoon winds slacken and to changes in the surface layer properties as the Arabian Sea cools and exports high-salinity Arabian Sea Water. The stratification was much weaker in September, with the depth of the top of the pycnocline deeper than the mixed layer over most of the section and by more than 100 m at the western boundary. The wind-driven flow extended down to the top of the pycnocline, and the Ekman temperature and salinity were colder and marginally less saline than surface values. The transport-weighted temperature (25.8 ± 0.5°C) was 1.1°C colder than the surface value, and the transport-weighted salinity (35.83 ± 0.03 psu) was not significantly different from the surface value of 35.86 psu. This resulted in a 5% decrease in the Ekman temperature transport over that calculated using the surface temperature.

The Ekman temperature flux appears to dominate the heat budget of the Indian Ocean north of 20°S (Levitus, 1987; Wacongne and Pacanowski, 1996; Garternicht and Schott, 1997). Since the Ekman temperature flux is sensitive to assumptions about the depth of penetration of the wind-driven flow, the Ekman depth is an important issue for the meridional overturning circulation of the Indian Ocean. We used the direct estimates of Ekman transport to compare various assumptions used in the literature regarding the Ekman depth: the surface mixed layer (e.g., Levitus, 1987), a fixed depth of 50 m (e.g., Hall and Bryden, 1982; Stramma et al., 2001), and the top of the pycnocline (e.g., Wijffels et al., 1996). For this pair of sections, we found that the top of the pycnocline did a good job of capturing the depth of wind mixing and in the vertical weighting of the Ekman temperature and salinity. In the absence of direct estimates of ageostrophic currents, the top of the pycnocline appears to be a better proxy for the Ekman depth than either the mixed layer or a fixed depth. This confirms the conclusion of Wijffels et al. (1996) for their section at 10°N in the Pacific, although the Arabian Sea sections provide a better test because there is a bigger dynamic range in the Ekman temperature. Although uncertainty in the Ekman mass transport dominates the error in the Ekman heat and salt fluxes, determining the Ekman depth is important in estimating the Ekman contribution to the heat budget of the tropical Indian Ocean.

Acknowledgements

The R.V. *Knorr* and R.V. *Baldridge* transects were supported by the National Science Foundation (NSF) and the National Oceanic and Atmospheric Administration (NOAA), respectively. We thank the chief scientists on I1 (Harry Bryden and John Morrison) and IR1 (Amy Ffield) for use of the CTD data, John Kindle for providing us with the NOGAPS wind data, and Carolyn Harris for help with some of the calculations. Margaret Yelland graciously provided us with results from the air-flow distortion study of the R.V. *Knorr*. The maps of sea level anomalies (MLSA) were generated by the AVISO group from TOPEX/POSEIDON and ERS satellite altimetry observations http://www-aviso.cls.cnes.fr. Comments from the anonymous reviewers improved the manuscript. Support from NSF Grants OCE94-13174 and OCE99-06776 is gratefully acknowledged.

Appendix A

Ship-relative wind speed and direction at 1-min intervals on the R.V. *Knorr* were made from a wind sensor on an Improved Meteorological Recorder or IMET (Hosom et al., 1995) located forward on the bow about 16 m above sea level. The wind direction is measured relative to the ship; the winds are rotated into a geographic reference frame using measurements of the ship's heading. We used the ship's gyrocompass corrected by the Ashtech (GPS heading) estimates. Ship velocity over the ground was subtracted to yield the absolute wind velocity. An overall misalignment (scale factor and angle) can be determined for absolute winds in the same manner as is done for ADCP measurements. No additional angle correction was made. However, we noticed a bias in the wind during the interval when the winds were strongest, from September 12–14. During this period, there was a mismatch between the absolute wind during steaming and station intervals that could not be accounted for by a rotation of the ship-relative winds. Yelland et al. (1998) report errors in wind speed measured from ships as large as 14% resulting from flow distortion in the air flow over the ship. The error is a function of sensor location, wind speed, and relative wind direction. Moat and Yelland (Airflow distortion at instrument sites on the R.V. *Knorr*, unpublished report, 1998) investigated the air flow around the R.V. *Knorr* using a computational fluid dynamics software package that simulated a flow of air directly over the bow of the ship. Due to the expense of the computation, only a single simulation was run: a 10-m wind of $15\,\mathrm{m\,s^{-1}}$ at zero relative angle measured by sensors in various locations on the ship, including an IMET wind sensor at 16 m height on the bow. This approximated the on-station configuration of the R.V. *Knorr*, which was turned into the currents and winds. The model-computed bias was −2.3%, i.e., flow distortion decelerated the wind at the IMET site by about 2%, much smaller than the effect that we observed. Wind direction was fairly steady for the period September 12–14 and the relative wind angle was about 50° while underway. Because the winds on station compared well with winds from the Navy Operational Global Atmospheric Prediction System (NOGAPS), and because NOGAPS winds compared well with those measured on the Baldridge, with the Arabian Sea mooring at 15°N (Weller et al., 1996), and with the remainder of the R.V. *Knorr* cruise (September 15–26), we applied a scale factor correction of 0.89 to the ship-relative winds during the steaming intervals for the period from September 12 to 14.

References

Beal, L.M., Chereskin, T.K., 2001. The volume transport of the Somali Current during the 1995 southwest monsoon. Deep-Sea Research II, submitted for publication.

Bruce, J.G., 1968. Comparison of near surface dynamic topography during the two monsoons in the western Indian Ocean. Deep-Sea Research I 15, 665–677.

Bruce, J.G., 1979. Eddies off the Somali coast during the southwest monsoon. Journal of Geophysical Research 84, 7742–7748.

Chereskin, T.K., Roemmich, D., 1991. A comparison of measured and wind derived Ekman transport at 11°N in the Atlantic Ocean. Journal of Physical Oceanography 21, 869–878.

Chereskin, T.K., Harding, A.J., 1993. Modelling the performance of an acoustic Doppler current profiler, 1993. Journal of Atmospheric and Oceanic Technology 10, 41–63.

Chereskin, T.K., Wilson, W.D., Bryden, H.L., Ffield, A., Morrison, J., 1997a. Observations of the Ekman balance at 8°30′N in the Arabian Sea during the 1995 southwest monsoon. Geophysical Research Letters 24, 2541–2544.

Chereskin, T.K., Harris, C.L., Trunnell, M., 1997b. Shipboard acoustic Doppler current profiling during the WOCE Indian Ocean Expedition: I1. Scripps Institution of Oceanography Reference Series, SIO-97-8, 226pp.

Cox, M.D., 1979. A numerical study of Somali Current eddies. Journal of Physical Oceanography 9, 311–326.

Düing, W., Leetmaa, A., 1980. Arabian Sea cooling: a preliminary heat budget. Journal of Physical Oceanography 10, 307–312.

Ffield, A., Fleurant, C., Molinari, R., Wilson, D., 1998. NOAA Ship MALCOLM BALDRIDGE 1995 cruises: MB95-02, MB95-04, MB95-07. Lamont Doherty Earth Observatory Technical Report LDEO-98-1, 322pp.

Findlater, J., 1969. A major low level air current near the Indian Ocean during the northern summer. Quarterly Journal of the Royal Meteorological Society 95, 365–380.

Fischer, J., Schott, F., Stramma, L., 1996. Currents and transports of the Great Whirl-Socotra Gyre system during the summer monsoon, August 1993. Journal of Geophysical Research 101, 3573–3587.

Garternicht, U., Schott, F., 1997. Heat fluxes of the Indian Ocean from a global eddy-resolving model. Journal of Geophysical Research 102, 21,147–21,159.

Hall, M.M., Bryden, H.L., 1982. Direct estimates and mechanisms of ocean heat transport. Deep-Sea Research I 29, 339–359.

Hellerman, S., Rosenstein, M., 1983. Normal monthly wind stress over the world ocean with error estimates. Journal of Physical Oceanography 13, 1093–1104.

Hosom, D.S., Weller, R.A., Payne, R.E., Prada, K.E., 1995. The IMET (improved meterology) Ship and Buoy systems. Journal of Atmospheric and Oceanic Technology 12, 527–540.

Josey, S.A., Kent, E.C., Oakley, D., Taylor, P.K., 1996. A new global air-sea heat and momentum flux climatology. International WOCE Newsletter 24, pp. 3–5.

Large, W.G., Pond, S., 1981. Open ocean momentum flux measurements in moderate to strong winds. Journal of Physical Oceanography 11, 324–336.

Levitus, S., 1987. Meridional Ekman heat fluxes for the world oceans. Journal of Physical Oceanography 17, 1484–1492.

Lighthill, M.J., 1969. Dynamic response of the Indian Ocean to the onset of the southwest monsoon. Philosophical Transactions of the Royal Meteorological Society A265, 45–92.

Morrison, J.M., 1997. Inter-monsoonal changes in the T-S properties of the near-surface waters of the northern Arabian Sea. Geophysical Research Letters 24, 2553–2556.

Prasanna Kumar, S., Prasad, T.G., 1999. Formation and spreading of Arabian Sea high-salinity water mass. Journal of Geophysical Research 104, 1455–1464.

Schott, F., Quadfasel, D., 1982. Variability of the Somali Current and associated upwelling. Progress in Oceanography 12, 357–381.

Schott, F., Swallow, J.C., Fieux, M., 1990. The Somali Current at the equator: annual cycle of currents and transports in the upper 1000 m and connection to neighboring latitudes. Deep-Sea Research I 37, 1825–1848.

Schott, F., Fischer, J., Garternicht, U., Quadfasel, D., 1997. Summer monsoon response of the northern Somali Current, 1995. Geophysical Research Letters 24, 2565–2568.

Schott, F.A., McCreary Jr., J.P., 2001. The monsoon circulation of the northern Indian Ocean. Progress in Oceanography 51 (1), 1–123.

Shankar, D., Shetye, S.R., 1997. On the dynamics of the Lakshadweep high and low in the southeastern Arabian Sea. Journal of Geophysical Research 102, 12,551–12,562.

Shetye, S.R., Gouveia, A.D., Shenoi, S.S.C., Sundar, D., Michael, G.S., Aleida, A.M., Santanam, K., 1990. Hydrography and circulation off the west coast of India during the Southwest Monsoon 1987. Journal of Marine Research 48, 359–378.

Shi, W., Morrison, J.M., Bryden, H.L., 2001. Water, heat, and freshwater flux out of the northern Indian Ocean in September—October 1995. Deep-Sea Research II, submitted for publication.

Stramma, L., Brandt, P., Schott, F., Quadfasel, D., Fischer, J., 2001. Winter and summer monsoon water mass and heat transport changes in the Arabian Sea near 8°N. Deep-Sea Research II, submitted for publication.

Wacongne, S., Pacanowski, R., 1996. Seasonal heat transport in a primitive equations model of the tropical Indian Ocean. Journal of Physical Oceanography 26, 2666–2698.

Weller, R.A., Baumgartner, M.F., Josey, S.A., Fischer, A.S., Kindle, J.C., 1996. Atmospheric forcing in the Arabian Sea during 1994-1995: observations and comparisons with climatology and models. Deep-Sea Research Part II 45, 1961–1999.

Wijffels, S., Firing, E., Bryden, H., 1994. Direct observations of the Ekman balance at 10°N in the Pacific. Journal of Physical Oceanography 24, 1666–1679.

Wijffels, S.E., Toole, J.M., Bryden, H.L., Fine, R.A., Jenkins, W.J., Bullister, J.L., 1996. The water masses and circulation at 10°N in the Pacific. Deep-Sea Research I 43, 501–544.

Yelland, M.J., Moat, B.I., Taylor, P.K., Hutchings, J., Cornell, V.C., 1998. Wind stress measurements from the open ocean corrected for airflow distortion by the ship. Journal of Physical Oceanography 49, 1511–1526.